

# A Comparison of the Water Budgets between Clouds from AMMA and TWP-ICE

XIPING ZENG AND WEI-KUO TAO

*Mesoscale Atmospheric Processes Laboratory, NASA Goddard Space Flight Center, Greenbelt, Maryland*

SCOTT W. POWELL AND ROBERT A. HOUZE JR.

*Department of Atmospheric Sciences, University of Washington, Seattle, Washington*

PAUL CIESIELSKI AND NICK GUY

*Department of Atmospheric Science, Colorado State University, Fort Collins, Colorado*

HAROLD PIERCE AND TOSHIHISA MATSUI

*Mesoscale Atmospheric Processes Laboratory, NASA Goddard Space Flight Center, Greenbelt, Maryland*

(Manuscript received 15 February 2012, in final form 11 September 2012)

## ABSTRACT

Two field campaigns, the African Monsoon Multidisciplinary Analysis (AMMA) and the Tropical Warm Pool–International Cloud Experiment (TWP-ICE), took place in 2006 near Niamey, Niger, and Darwin, Northern Territory, Australia, providing extensive observations of mesoscale convective systems (MCSs) near a desert and a tropical coast, respectively. Under the constraint of their observations, three-dimensional cloud-resolving model simulations are carried out and presented in this paper to replicate the basic characteristics of the observed MCSs. All of the modeled MCSs exhibit a distinct structure having deep convective clouds accompanied by stratiform and anvil clouds. In contrast to the approximately 100-km-scale MCSs observed in TWP-ICE, the MCSs in AMMA have been successfully simulated with a scale of about 400 km.

These modeled AMMA and TWP-ICE MCSs offer an opportunity to understand the structure and mechanism of MCSs. Comparing the water budgets between AMMA and TWP-ICE MCSs suggests that TWP-ICE convective clouds have stronger ascent while the mesoscale ascent outside convective clouds in AMMA is stronger. A case comparison, with the aid of sensitivity experiments, also suggests that vertical wind shear and ice crystal (or dust aerosol) concentration can significantly impact stratiform and anvil clouds (e.g., their areas) in MCSs. In addition, the obtained water budgets quantitatively describe the transport of water between convective, stratiform, and anvil regions as well as water sources/sinks from microphysical processes, providing information that can be used to help determine parameters in the convective and cloud parameterizations in general circulation models (GCMs).

## 1. Introduction

Mesoscale convective systems (MCSs), a common weather phenomenon in the tropics (e.g., Mohr and Zipser 1996; Schumacher and Houze 2006; Yuan and Houze 2010), consist of convective, stratiform, and anvil clouds (e.g., Houze 1977; Zipser 1977). Convective clouds therein become organized into cloud clusters that in turn

generate cloud shields (or stratiform and anvil clouds) in their mature and later stages (Zipser 1969; Houze 1977, 1982). Since cloud shields are widespread ( $10^4$ – $10^5$  km<sup>2</sup> in area; Houze 1982; Nesbitt et al. 2000), they modulate atmospheric radiation and consequently impact large-scale vertical circulations as well as radiative forcing (e.g., Houze 1982; Zeng et al. 2009a). However, many issues remain regarding MCSs [see Houze (2004) for review], such as the factors that determine their geographic distribution (e.g., Yuan and Houze 2010).

Two field campaigns, the African Monsoon Multidisciplinary Analysis (AMMA) and the Tropical Warm Pool–International Cloud Experiment (TWP-ICE), took

---

*Corresponding author address:* Dr. Xiping Zeng, C423, Bldg. 33, Mail Code 612, NASA Goddard Space Flight Center, Greenbelt, MD 20771.  
E-mail: xiping.zeng@nasa.gov

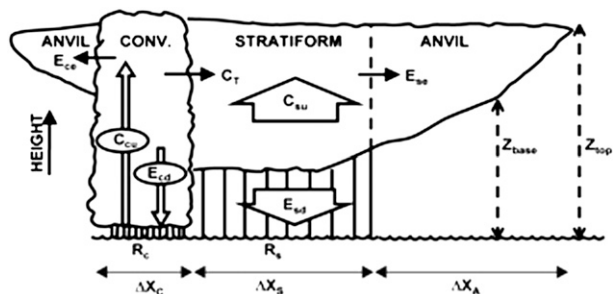


FIG. 1. Schematic vertical cross section of an idealized MCS with convective region (CONV.), associated stratiform precipitation region, and nonprecipitating cirriform anvil. Adapted from Houze et al. (1980). The horizontal dimensions of the convective, stratiform, and anvil regions are indicated by  $\Delta x_C$ ,  $\Delta x_S$ , and  $\Delta x_A$ , respectively. The various terms in the schematic represent sources and sinks of condensate in the convective, stratiform, and anvil regions. These terms represent the amount of convective region condensation  $C_{cu}$  and the portions of the convective region condensation that are rained out  $R_c$ , evaporated in the convective downdrafts  $E_{cd}$ , detrained to an anvil  $E_{ce}$ , and transported into the stratiform region  $C_T$ . Condensate in the stratiform region includes  $C_T$  plus the amount of condensate generated by the stratiform updraft  $C_{su}$ . Part of  $(C_T + C_{su})$  is rained out  $R_s$ , part is evaporated into the downdraft  $E_{sd}$ , and part is detrained to or left aloft in a thick anvil or ice cloud  $E_{se}$ .

place in 2006 near Niamey, Niger, and Darwin, Northern Territory, Australia, providing extensive observations of MCSs near a desert and a tropical coast, respectively (Redelsperger et al. 2006; May et al. 2008). Under the constraint of the observations, cloud-resolving model (CRM) simulations are carried out first to characterize, as examples, the differences between MCSs from the two campaign locations and then to infer the possible factors that impact the geographic distribution of MCSs.

The water budget for an MCS describes the transport of water between convective, stratiform, and anvil cloud regions as well as water source(s)/sink(s) from microphysical processes. Figure 1 displays a schematic of an MCS water budget from Houze et al. (1980). The terms in the schematic have been discussed using observational data (e.g., Houze 1977; Zipser et al. 1981; Gamache and Houze 1983; Rutledge and Houze 1987; Johnson and Hamilton 1988; Frederick and Schumacher 2008; Guy et al. 2011) and CRM simulations (e.g., Tao et al. 1993; Chin 1994; Caniaux et al. 1994; Lang et al. 2003), revealing some important factors in a water budget such as vertical wind shear and the depositional growth associated with upward motion [see Tao (2003) for review].

Recent high-quality observational datasets from AMMA and TWP-ICE as well as three-dimensional (3D) CRM simulations offer a new opportunity to study MCS water budgets. Since dust particle amounts are higher in AMMA than in TWP-ICE, can the difference in the water budgets

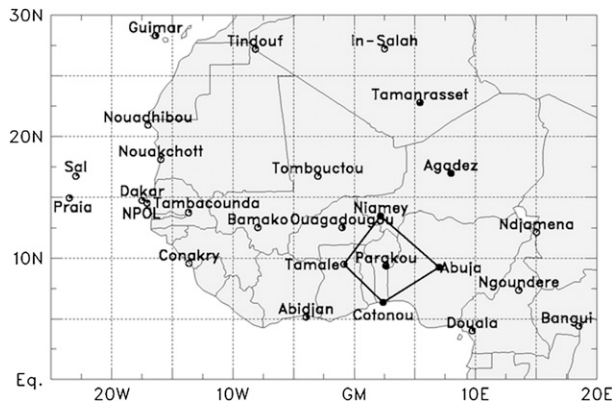


FIG. 2. Field campaign stations for AMMA and NASA AMMA (NAMMA). Observational data from Niamey, Tamale, Cotonou, Abuja, and Parakou during the SOP are used to drive the present AMMA CRM simulations.

between AMMA and TWP-ICE MCSs be attributed (partially) to the difference in dust aerosols? With this question in mind, the water budget analysis is revisited in the present paper following Tao et al. (1993).

The paper consists of six sections. In section 2, the field campaigns and the CRM used are briefly introduced. In section 3, AMMA and TWP-ICE numerical simulations are described and their results are compared with radar and satellite observations. In section 4, the water budgets from the AMMA simulations are analyzed and contrasted with those from the TWP-ICE simulations. In section 5, the effects of vertical wind shear and ice crystal concentration on MCSs are addressed by comparing the AMMA and TWP-ICE simulations. Concluding remarks are offered in section 6.

## 2. Setup for the AMMA and TWP-ICE simulations

### a. Observations of AMMA and TWP-ICE MCSs

Observations from field campaigns (in this case, AMMA and TWP-ICE) can be used to drive and evaluate CRM simulations. AMMA was a large international project undertaken to improve the understanding of the West African monsoon (e.g., Redelsperger et al. 2006). Its special observing period (SOP) focused on specific processes and weather systems near Niamey, Niger, between 1 June and 15 September 2006. Figure 2 shows the sounding network during the AMMA SOP. The results for AMMA presented in this paper focus on the budget network consisting of five sounding stations: Niamey, Tamale, Cotonou, Abuja, and Parakou (indicated with a polygon in Fig. 2). During the SOP, 4 day<sup>-1</sup> sonde observations were taken at these sites except for two 2-week periods in which the sonde launch frequency

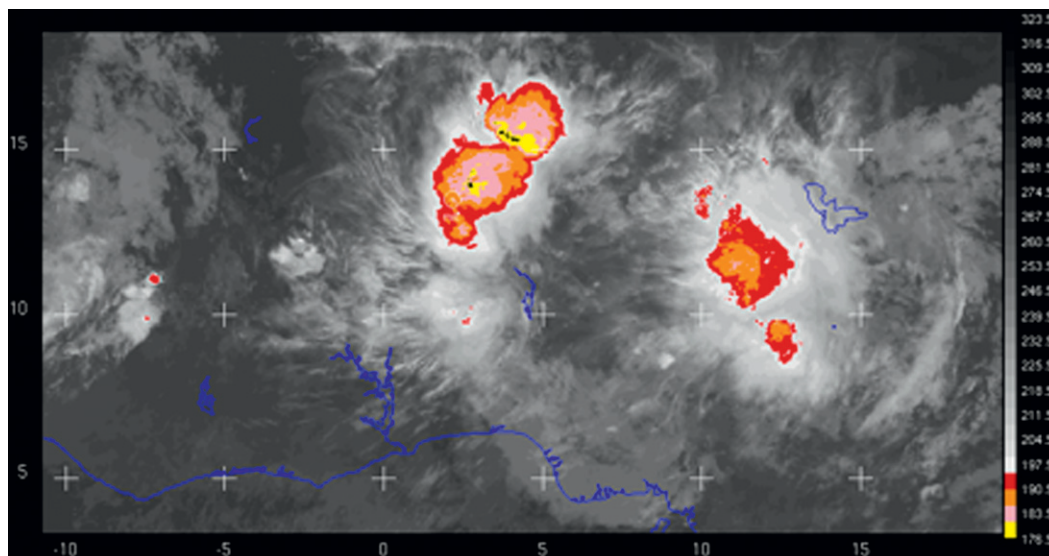


FIG. 3. *Meteosat-8* infrared brightness temperature at 0319 UTC 11 Aug 2006. The MCS on the left is simulated in the paper.

was increased to  $8 \text{ day}^{-1}$ . Soundings from this network were corrected for humidity biases as described in Nuret et al. (2008) and were quality controlled as in Loehrer et al. (1996). This sounding budget array encloses an area of about  $600 \text{ km}^2$  with its center near  $(9^\circ\text{N}, 2.5^\circ\text{E})$ . Owing to the large amounts of dust present in the northern vicinity of the SOP network (e.g., Zipser et al. 2009), observations in this region are ideal for investigating the effects of dust aerosols on MCSs.

The two MCSs chosen for study in this paper swept westward over the sounding network on 18–19 July and 10–11 August 2006, respectively. The two systems were well organized and had a distinct structure with deep convective clouds accompanied by stratiform clouds and nonprecipitating ice anvil clouds (Cetrone and Houze 2011; Powell et al. 2012). Their structure was captured well by observations from the radars at Niamey as well as *CloudSat* (Stephens et al. 2002) and the Tropical Rainfall Measuring Mission (TRMM) satellite. The MCS on 10–11 August, for example, is described here briefly

to summarize the basic characteristics of MCSs in the AMMA region. A *Meteosat-8* infrared (IR) brightness temperature at 0319 UTC 11 August 2006 is shown in Fig. 3. It exhibits two MCSs. The left one, which crossed the sounding network, is modeled in this paper. This MCS was captured by the W-band Atmospheric Radiation Measurement (ARM) cloud radar located at Niamey as it passed over the radar. It exhibited clear leading and trailing anvils, and since the MCS propagated westward over the radar, an effective east–west vertical cross section of the MCS was obtained (Powell et al. 2012). *CloudSat* flew southward over the MCS at about 0131 UTC 11 August 2006, obtaining a north–south vertical cross section of attenuating W-band radar reflectivity across the MCS. Figure 4 displays the vertical cross section from *CloudSat* and shows that the MCS had an anvil that extended on the order of 400 km.

The TRMM satellite flew over the easternmost of the two MCSs shown in Fig. 3 at about 0433 UTC 11 August 2006, providing a reference for the western MCS that is

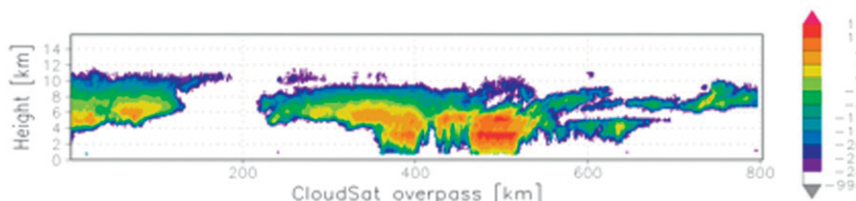


FIG. 4. Vertical cross section of attenuating W-band radar reflectivity (dBZ) from *CloudSat* at about 0131 UTC 11 Aug 2006. The image corresponds to the satellite overpass from  $13^\circ\text{N}, 5^\circ\text{E}$  at 0131 UTC on the left side to  $6^\circ\text{N}, 3.5^\circ\text{E}$  at 0133 UTC 11 Aug 2006 on the right side.

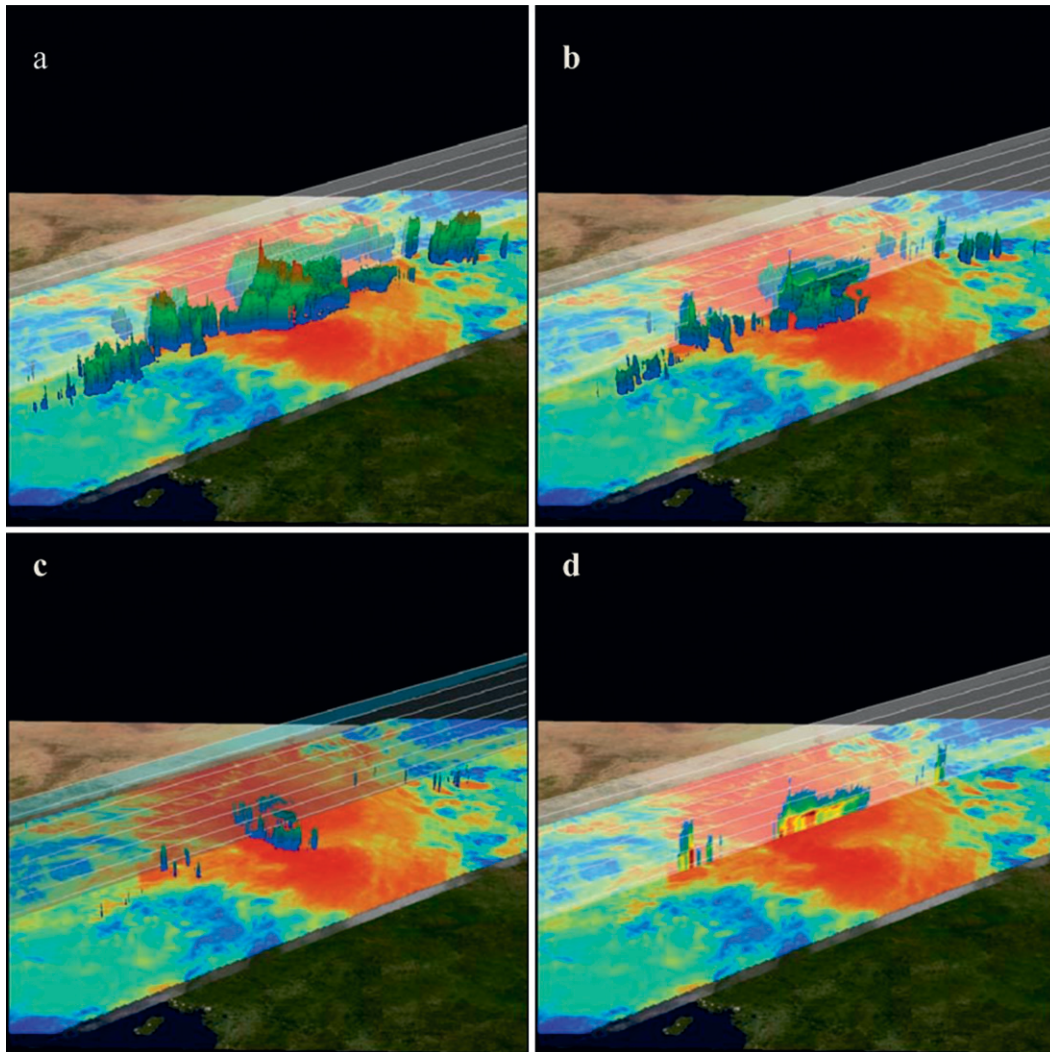


FIG. 5. (a)–(c) Three-dimensional images from TRMM satellite PR data received at about 0433 UTC 11 Aug 2006 over west-central Africa. They are overlaid on an infrared image from TRMM’s Visible and Infrared Scanner (VIRS) instrument. Temperature values range from red for the coldest to blue for the warmest. White lines, drawn at an interval of 2.5 km, show the height of TRMM PR features. The top line indicates an altitude of 20 km. The surfaces of cloud tops defined as (a) 15, (b) 30, and (c) 40 dBZ, respectively. (d) A vertical cross section of reflectivity values within the highest cloud.

modeled here. The TRMM Precipitation Radar (PR) provided data for 3D images of convective clouds in the MCS. Figure 5 displays cloud-top surfaces at 15, 30, and 40 dBZ, respectively. As the magnitude of reflectivity increases, the cores of convective clouds become separated from their neighbors. Such separation in convective cells is also clear in the vertical cross section of radar reflectivity shown in Fig. 5 as well as the hourly IR images from the geostationary satellite *Meteosat-8*. This suggests that the MCS was generated by horizontally separated convective cells although the cells had a tendency to be organized within the MCS. This separation in convective cells resembles “connected active MCSs,”

which is an MCS subcategory of Yuan and Houze (2010), where active convective systems are separated but their precipitation areas are connected (Houze 1997).

The MCSs observed in AMMA are different from those in TWP-ICE (e.g., Protat et al. 2010). TWP-ICE was conducted around Darwin, Northern Territory, Australia, in January and February of 2006 during the northern Australian monsoon (May et al. 2008). Its sounding network enclosed a region with a scale of 210 km centered at 12°S, 131°E (e.g., Xie et al. 2010). Several squall lines, which occur in a typical monsoon break period, crossed the sounding network from 4 to

12 February 2006. Radar observations show that the MCSs during this period had a scale of about 100 km (Frederick and Schumacher 2008), which is much smaller than those from AMMA shown in Figs. 3–5. Since National Aeronautics and Space Administration (NASA) satellite observations ([http://eosweb.larc.nasa.gov/HPDOCS/misr/misr\\_html/global\\_aerosols.html](http://eosweb.larc.nasa.gov/HPDOCS/misr/misr_html/global_aerosols.html)) show that the dust concentrations near Niamey in summer are much higher than those near Darwin in spring, the MCSs observed in AMMA and TWP-ICE are modeled here with a CRM to investigate the effects of aerosols on the MCSs.

### b. Model setup

The Goddard CRM (e.g., Tao and Simpson 1993; Tao et al. 2003) is used in this study to simulate the MCSs. The model is nonhydrostatic and anelastic. It has an option to change cloud microphysics from the three-class ice formulations of Rutledge and Hobbs (1984) to a bin microphysical representation. It takes account of the absorption/scattering for solar radiation and the emission/absorption of infrared radiation. Its cloud-radiation interaction has been assessed (Tao et al. 1996). Subgrid-scale (turbulent) processes in the model are parameterized using a scheme based on Klemp and Wilhelmson (1978) and Soong and Ogura (1980). The effects of both dry and moist processes on the generation of subgrid-scale kinetic energy have been incorporated. All scalar variables (temperature, water vapor, and all hydrometeors) are calculated with a positive definite advection scheme (Smolarkiewicz and Grabowski 1990). Model results can be used to mimic radar and satellite observations using the Goddard Satellite Data Simulator Unit (G-SDSU), and subsequently be compared with radar and satellite observations (Matsui et al. 2009).

The model in the paper has the same structure as that in previous studies (e.g., Grabowski et al. 1996, 1998; Xu and Randall 1996; Wu et al. 1999; Wu and Moncrieff 2001; Johnson et al. 2002; Xu et al. 2005; Blossey et al. 2007; Zeng et al. 2011). The observed large-scale horizontal and vertical advection terms of potential temperature and water vapor mixing ratio are used to drive model simulations (e.g., Grabowski et al. 1996; Wu et al. 1999). The horizontal wind components in the model are relaxed to the observed so that the vertical wind shear for clouds is accurate (e.g., Grabowski et al. 1996; Xu and Randall 1996).

Three numerical experiments analyzed in the paper are listed in Table 1. All of the numerical experiments are 3D, using a 1-km horizontal grid spacing and the microphysical scheme based on Rutledge and Hobbs (1984) with the addition of ice crystal concentration (Zeng et al. 2008). The model therefore has five prognostic hydrometeor variables: the mixing ratios of cloud

TABLE 1. Numerical experiments.

Experiment	Field campaign	Date	Grid points
M0811MH	AMMA	10–11 Aug 2006	1024 × 1024 × 63
M0719MH	AMMA	18–19 Jul 2006	1024 × 1024 × 63
T06MH	TWP-ICE	4–12 Jan 2006	256 × 256 × 41

water, rainwater, cloud ice, snow, and graupel. Ice crystal concentration is also introduced as an input factor. The ice crystal concentration in the TWP-ICE numerical experiment is assigned such that the modeled water species agree with radar observations (Zeng et al. 2011). The same value is used in the AMMA experiments so that the modeled ice water contents are also close to those derived from the W-band radar observations (see section 3b for further discussion).

The three numerical experiments for TWP-ICE and AMMA follow the same model setup except for the forcing because of the different sounding networks. The TWP-ICE experiment (or T06MH) uses 41 layers with vertical resolution ranging from 42.5 m at the bottom to 1 km at the model top. It uses 256 × 256 × 41 grid points to cover the region surrounded by the TWP-ICE sounding network. In contrast, the two AMMA numerical experiments (i.e., M0719MH and M0811MH) use 1024 × 1024 × 63 grid points to cover the region surrounded by the AMMA sounding network and to allow a vertical resolution of 300 m in the upper troposphere to better resolve anvil clouds.

The forcing data used in the TWP-ICE and AMMA numerical experiments come from their corresponding field campaigns, respectively. The AMMA forcing data were derived from 6-hourly observations at the five network sounding sites shown in Fig. 2. Since it is difficult to obtain accurate mean spatial surface fluxes over the entire budget arrays for long-term CRM simulations (Zeng et al. 2007), the horizontally averaged temperature and humidity at the lowest three model levels (378.5-m layer) are relaxed to the observed values with a time scale of about 10 min. Specifically, a scalar variable  $\phi$  (i.e., potential temperature or the mixing ratio of water vapor) is relaxed to  $\phi_{\text{obs}}$  the observed value from the sounding network via an additional source term. That is,

$$\partial\phi/\partial t = \dots - (\bar{\phi} - \phi_{\text{obs}})/\tau,$$

where  $\bar{\phi}$  is the horizontal average of  $\phi$  and  $\tau$ , the time scale for relaxation. In the present simulations,  $\tau = 10 \times [200/(\bar{p} - 800)]$  minutes when  $\bar{p} > 800$  hPa, where  $\bar{p}$  represents the horizontal average of atmospheric pressure. This relaxation is sufficiently strong that the model results are not sensitive to the imposed

surface fluxes. Besides, the additional source term is horizontally uniform and consequently the relaxation does not restrain the simulation of  $\phi$  perturbations caused by convective downdrafts.

### 3. AMMA simulations

Two numerical experiments M0719MH and M0811MH are carried out to simulate two MCSs that occurred during AMMA on 18–19 July and 10–11 August 2006, which are referred to here as the 19 July and 11 August cases (or MCSs), respectively. The two numerical experiments start at 0600 UTC 18 July and 10 August 2006, respectively, and last for 30 h. Their initial condition is chosen based on satellite observations. Hourly stationary satellite images show that the 19 July MCS evolved as follows. Four individual convective systems (two smaller and two larger) reached the eastern edge of the sounding network at 0100 UTC 19 July 2006. The systems then merged to form a long MCS that became mature at 0400 UTC and dissipated thereafter. The 11 August MCS resembled the 19 July one. It swept over the sounding network with its southern part. It consisted of several small convective cloud systems in a line at 2119 UTC 10 August 2006 before reaching the northeastern edge of the network at 0019 UTC 11 August. It reached maturity (Leary and Houze 1979) at 0419 UTC and left the northwestern edge of the network at 0719 UTC.

To mimic the advection of convective systems into the sounding network, four warm bubbles are introduced into the model with a scale of 50 km in the right part of the domain. The bubbles are introduced gradually within the first 14 h with accumulated temperature perturbations of 4°C. Gradual introduction of the bubbles prevents the formation of strong artificial gravity waves. Next, the modeled MCSs are compared with satellite- and ground-based radar observations, respectively.

#### a. Comparison with satellite observations

Figure 6 displays the simulated rainfall rate in M0719MH from day 0.5 to 1.2. Also shown are rainfall estimates based on a TRMM satellite algorithm and sounding budget residuals. The satellite estimate comes from the TRMM 3B42v6 rainfall product (Huffman et al. 2007), which is available at 3-h intervals and 0.25° resolution. The high temporal resolution of this product is achieved by combining TRMM 2A-12, Special Sensor Microwave Imager (SSM/I), Advanced Microwave Scanning Radiometer (AMSR), and AMSR for Earth Observing System (AMSR-E) precipitation estimates along with hourly IR data from geostationary satellites. Generally speaking, the modeled rainfall rates agree well with

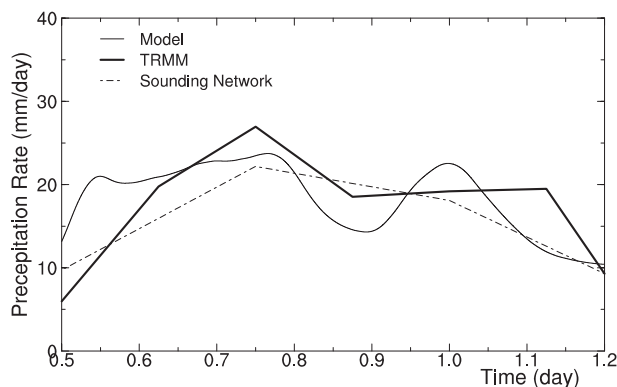


FIG. 6. Modeled and observed AMMA rainfall rates vs time starting at day 0.5 or 1800 UTC 18 Jul 2006. The thin line represents the modeled results. The thick solid and dashed lines denote the results derived from the TRMM satellite and the sounding network, respectively.

the budget-derived estimates because the 19 July MCS developed within the sounding network. In contrast, the modeled rainfall rates in M0811MH do not agree well with the budget-derived estimates (not shown) because only the southern portion of the 11 August MCS crossed the sounding network.

Both of the AMMA numerical experiments are able to replicate the large observed MCSs. The modeled 11 August MCS is compared with observations in detail in the paper while the modeled 19 July MCS is used to provide additional background for the analysis. Figures 7 and 8 display a snapshot of M0811MH at 0400 UTC 11 August. Figure 7 displays the horizontal distribution of the modeled MCS in terms of cloud ice and graupel mixing ratios at a height of 8.6 and 5 km, respectively. The figure shows that the modeled MCS has a scale of 400 km. Since the cloud ice at 8.6 km and the graupel at 5 km approximately measure the cloud anvil and convective cores, respectively, the figure indicates that the modeled anvil/stratiform clouds are much larger in area than the convective cores. In addition, the modeled convective cells are separated horizontally, whereas they appear organized into two connected parts (or sub-MCSs) based on their precipitation areas. The two-sub-MCS pattern resembles the satellite image shown in Fig. 3.

Figure 8 displays the volumes of precipitating particles (i.e., rainwater, snow, and graupel) as well as cloud ice at 0400 UTC 11 August. Because of the cyclic boundary conditions in the model, in the figure, the first half of the domain is moved right after the second half in the east–west direction so as to provide a better 3D view of the clouds. Since the precipitating particles approximately represent convective- and precipitating-stratiform clouds and cloud ice represents anvil clouds,

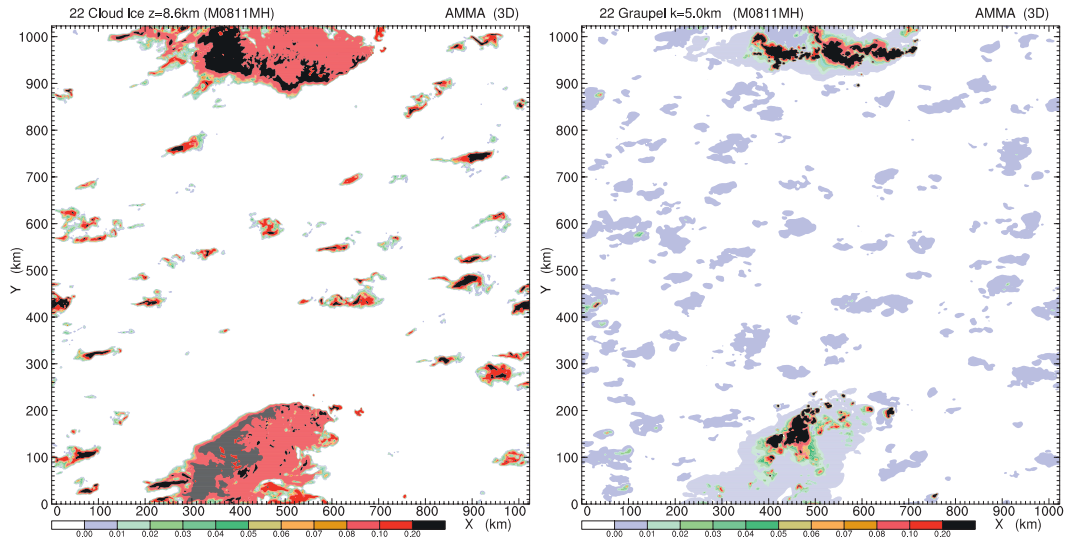


FIG. 7. Horizontal distribution of (left) cloud ice mixing ratio at 8.6 km and (right) graupel mixing ratio at 5 km at hour 22 or 0400 UTC 11 Aug 2006. The results come from experiment M0811MH.

the figure shows that deep convective cores (evidenced by overshooting domes) are horizontally separated but share the same cloud anvil, which resembles the satellite observations shown in Figs. 3–5. In addition, the modeled leading anvil is higher than the trailing one, just as was observed by the W-band radar (Powell et al. 2012). Strong reflectivity beyond the convective regions occurs below 5 km, which resembles the observations shown in Fig. 5 and the TRMM PR observations over West Africa (Cetrone and Houze 2009).

*b. Comparison with W-band radar observations*

Anvil clouds are further divided into thin, medium, and thick based on thicknesses of 0–2, 2–6, and >6 km, respectively (e.g., Yuan and Houze 2010; Cetrone and Houze 2011; Powell et al. 2012). Since the ARM W-band radar can detect anvil clouds with a high degree of sensitivity (e.g., –35 dBZ at 10 km), its data are used to characterize thin, medium, and thick anvils that can be used to evaluate the simulated anvils.

Anvil clouds are sensitive to the ice crystal concentration in the mixed-phase region (e.g., Zeng et al. 2009b). Thus, different ice crystal concentrations can be assigned in different CRM simulations in contrast to observations to infer the in situ ice crystal concentration (e.g., Zeng et al. 2009a, 2011; Morrison et al. 2011). Numerous sensitivity experiments have been performed with the same setup as M0811MH except for different ice crystal concentrations, indicating an increase in anvil ice water content with increasing ice crystal concentration (see section 5b for further discussion). When M0811MH is run with the same ice crystal concentration as was used in T06MH to properly duplicate TWP-ICE clouds, its modeled ice water content (IWC) in the anvil clouds is close to the observations. Figure 9 displays the vertical profiles of IWC modeled in thick, medium, and thin anvils. The profiles can be compared quantitatively with those derived from the W-band radar (Powell et al. 2012). The modeled IWC for thick anvil is quite close to the observational results shown in Powell et al. (2012),

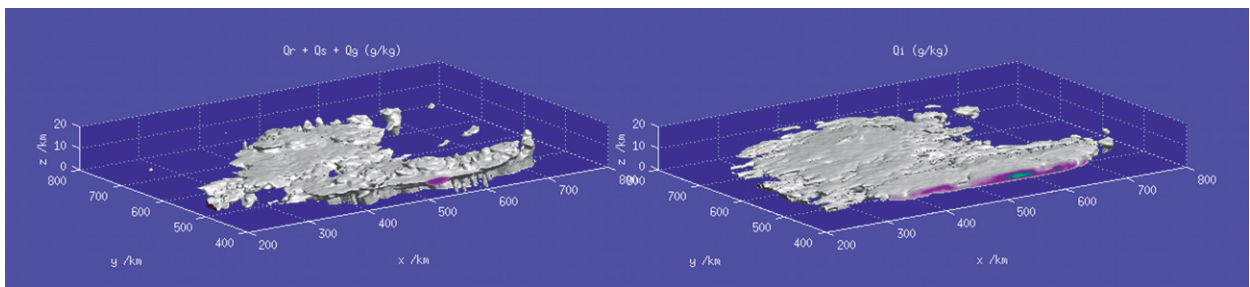


FIG. 8. A snapshot of the modeled AMMA clouds at 0400 UTC 11 Aug 2006 in experiment M0811MH. (left) The volume of precipitating particles, and (right) the volume of cloud ice, depicting the cloud anvil.

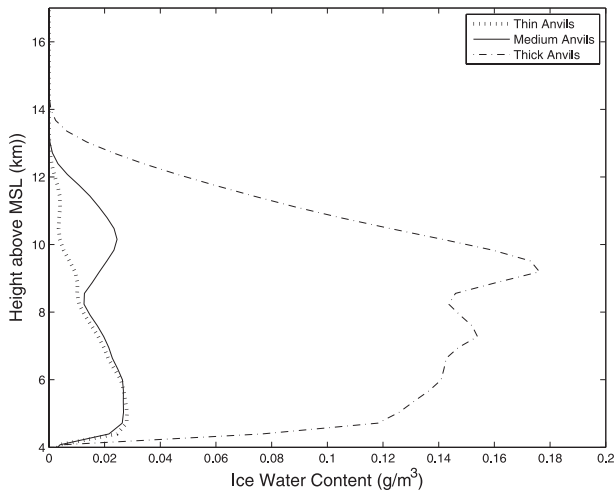


FIG. 9. Vertical profiles of ice water content in thick (dash-dotted), medium (solid), and thin anvils (dashed) in experiment M0811MH.

whereas modeled IWCs for thin and medium anvils are lower than observations in the upper troposphere (e.g., between 10 and 14 km).

#### c. Comparison with the TWP-ICE simulation

The TWP-ICE numerical experiment T06MH was introduced in Zeng et al. (2011). It is discussed here briefly to contrast against the AMMA experiments. T06MH was initialized at 2100 UTC 4 February 2006 and run for 8 days. Figure 10 displays a snapshot of the modeled clouds at 1424 UTC 11 February 2006, showing that the MCS had a scale of 100 km, which is close to the radar observations of Frederick and Schumacher (2008). The figure shows the volume of precipitating water particles (or the sum of rainwater, snow, and graupel mixing ratios) and nonprecipitating ones (or the sum of cloud water and ice mixing ratios) where the total

mixing ratio of water species at the surfaces is defined as 0.01 times its maximum value in the domain (i.e.,  $0.01 \text{ g kg}^{-1}$  for nonprecipitating particles and  $0.1 \text{ g kg}^{-1}$  for precipitating particles). Since precipitating particles are much larger in size than nonprecipitating ones, reflectivity associated with the precipitating particles is much larger than those for the latter. Hence, the two panels roughly depict convective clouds and the cloud shield, respectively. Generally speaking, the modeled TWP-ICE anvil clouds are much larger in area than convective clouds.

#### 4. Water budget analysis

In contrast to the preceding qualitative comparison between the modeled AMMA and TWP-ICE clouds, a quantitative comparison is presented in this section by analyzing the water budget. Following the schematic of Houze et al. (1980) in Fig. 1, the model domain is divided into convective, stratiform, and anvil (or nonprecipitating) cloud regions and clear sky (or the cloud environment). Two isothermal surfaces at temperatures of  $0^\circ$  and  $-35^\circ\text{C}$  are used to divide the troposphere into three layers: warm, mixed-phase, and icy cloud layers. As a result, the horizontal and vertical fluxes of all water species (except for water vapor) between the regions and layers can be computed as well as the sources of all water species owing to microphysics in each subregion (see the appendix for the water budget computation algorithm).

The convective–stratiform separation scheme used in the present study is the same as that in Churchill and Houze (1984) with two additional criteria: one on vertical velocity and another on cloud water content (Tao et al. 1993). Since 3D simulations generate larger vertical velocity than their two-dimensional (2D) counterparts (e.g., Phillips and Donner 2006; Zeng et al. 2008), two parameters in the two criteria are tuned for 3D

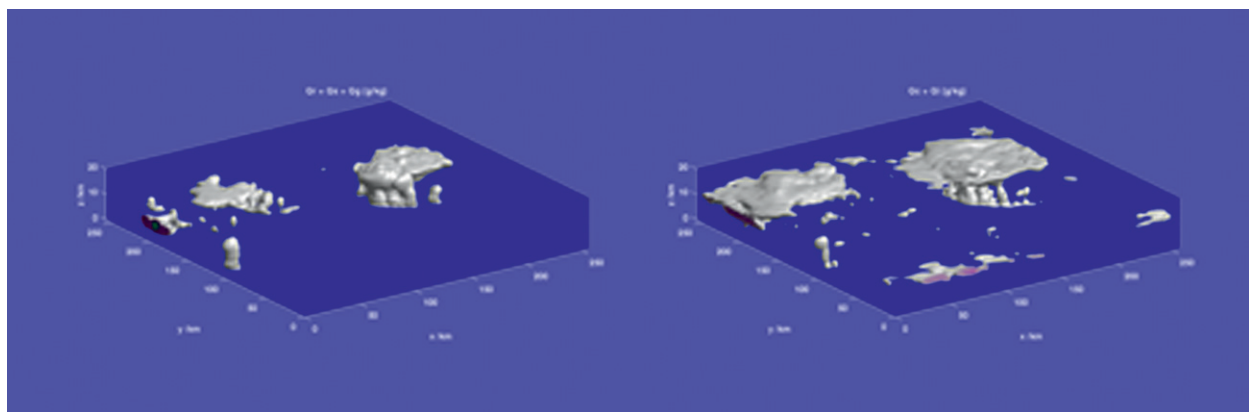


FIG. 10. A snapshot of the modeled TWP-ICE clouds at 1424 UTC 11 Feb 2006. The volume of (left) precipitating and (right) nonprecipitating particles.

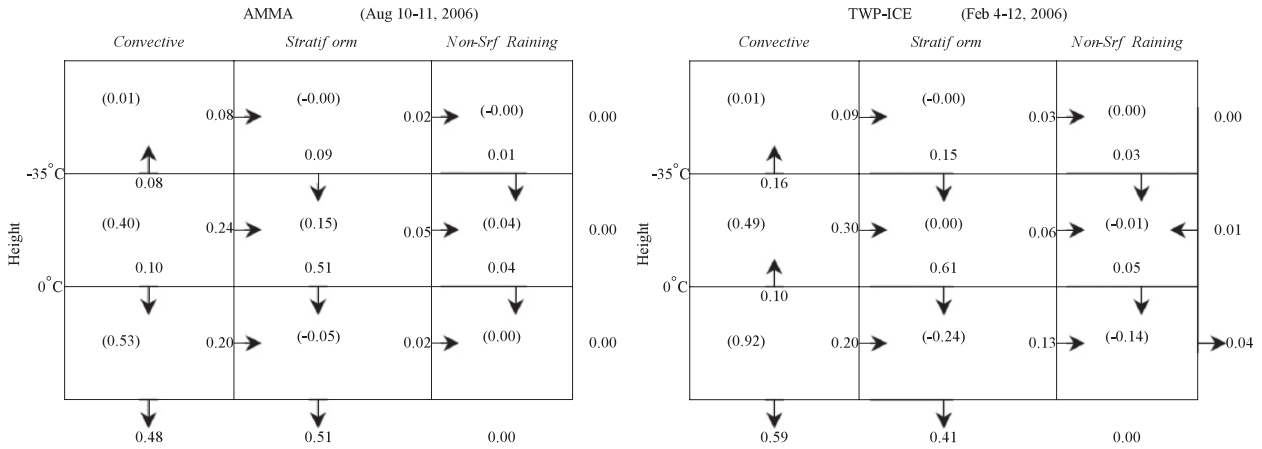


FIG. 11. Water budgets for (left) M0811MH and (right) T06MH. All of the quantities are normalized by the total surface precipitation. Horizontal arrows indicate water fluxes between the convective, stratiform, and anvil cloud regions, and vertical arrows the water fluxes between warm, mixed-phase, and icy cloud layers. Variables in boxes represent the water sources due to microphysical processes.

simulations so that the cloud separation in the model is close to that from radar observations (see the comparison in stratiform precipitation percentage below). Specifically, a pixel is made convective if cloud water exceeds a threshold of  $0.88 \text{ g kg}^{-1}$  below the melting level or  $1.76 \text{ g kg}^{-1}$  above the melting level, or if the updraft exceeds  $3 \text{ m s}^{-1}$ . Once the parameters are chosen, they change with neither clouds nor their stages so that results are comparative between cases.

In the present study, the water fluxes and microphysical water sources are computed every 5 min and then accumulated over the entire modeling period. Figure 11 displays the water budgets obtained for M0811MH and T06MH, where all variables are normalized by the total surface precipitation amount [or convective and stratiform precipitation ( $R_c + R_s$ ) in Fig. 1] for comparison.

The water budget for M0811MH, which is similar to that for M0719MH, is discussed here as being representative of Niamey. The modeled convective (stratiform) rain amount is 48.6% (51.4%), which is close to the 51% (49%) that was derived from C-band radar observations collected at Niamey during the AMMA SOP (Guy et al. 2011). In contrast, the modeled TWP-ICE convective (stratiform) rain amount in T06MH is 58.6% (41.4%). The difference in stratiform precipitation percentage between the AMMA and TWP-ICE cases is possible because stratiform precipitation percentage varies significantly from case to case (Cetrone and Houze 2009).

*a. Convective water budgets*

The convective water budgets in Fig. 11 are compared between T06MH and M0811MH to contrast the difference in their deep convection. The microphysical water source in the convective region in T06MH is stronger

than that in M0811MH. Since the microphysical water source measures the amount of vapor condensation/deposition, the difference in water source between the two experiments suggests that deep convection in T06MH is stronger than in M0811MH.

This conclusion on the difference in deep convection is supported by other water variables. The modeled vertical water fluxes at  $0^\circ$  and  $-35^\circ\text{C}$  in the convective region are larger in T06MH than in M0811MH. These modeling characteristics are attributed to stronger vertical velocities in the TWP-ICE convective clouds than those in the AMMA MCSs. Figure 12 displays probability density functions (PDFs) of vertical velocity  $w$  from T06MH and M0811MH; it shows that for strong vertical velocities (i.e., in the convective clouds), the frequency of occurrence is larger in T06MH than in M0811MH. Also, the height of the maximum vertical velocities (e.g., at  $10 \text{ m s}^{-1}$ ) is lower in T06MH than in M0811MH. These differences in the water variables and vertical velocities suggest that the convection in T06MH is stronger than in M0811MH and is consistent with the high level of lightning activity observed in the break-period storms near Darwin (May et al. 2008).

The budgets in Fig. 11 represent the ensemble average of all clouds in the numerical experiments. Suppose that all of the clouds in the model have the same structure as that in Fig. 1 with  $E_{ce} = 0.1$ . Water balance would be

<sup>1</sup> MCS propagation affects the computation of water budget. Figure 1 depicts the water budget on a framework that moves with the MCS. Suppose that the MCS in Fig. 1 is steady and propagates to the left. An advective water flux from a nonprecipitating to a convective region occurs in a stationary framework. This flux is directly proportional to the MCS propagation speed and the water content in the nonprecipitating region.

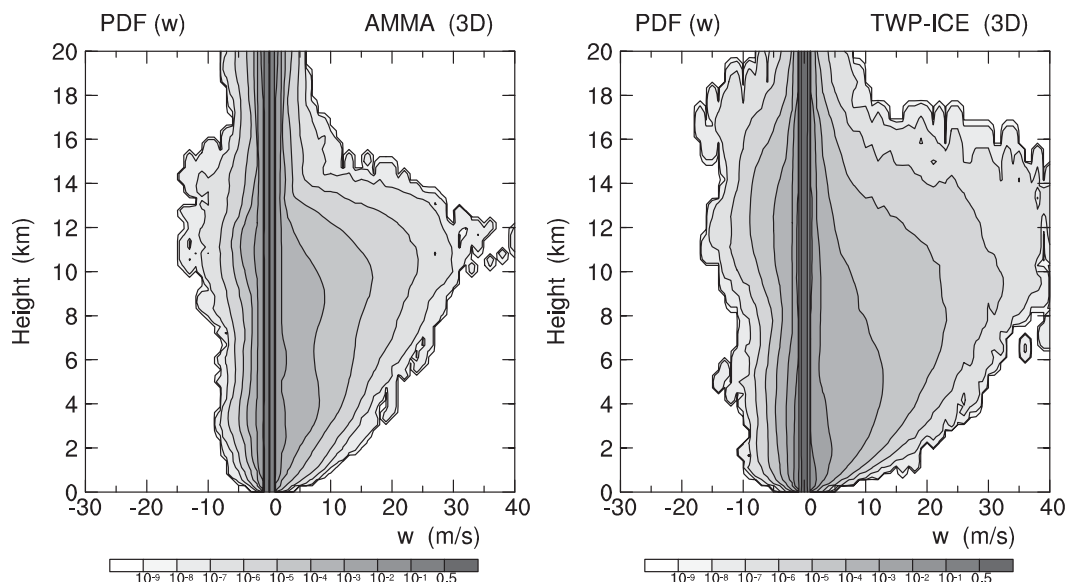


FIG. 12. PDFs of vertical velocity for (left) M0811MH and (right) T06MH.

expected in each region (i.e., box) in Fig. 11: outward minus inward water fluxes would equal the microphysical water source inside. However, the clouds in the model include not only MCSs but also non-MCS clouds such as isolated convective clouds that can transport water directly to the nonprecipitating cloud region and/or the cloud environment. As a result, water “imbalance” arises in some of the regions in Fig. 11.

The water imbalance in the convective regions approximately measures the contribution of non-MCS clouds to the water budget. Looking at the water budget in the convective region for T06MH, for example, there is balance in the warm cloud layer but not above it. To be specific, 27% of the water source (or 0.13/0.49) in the mixed-phase cloud layer flows out into the nonprecipitating cloud region and/or the cloud environment, and 38% of the water (or 0.06/0.16) that is transported from the mixed-phase to the icy layer flows out into the nonprecipitating cloud region. This difference in the water budget implies that about one quarter of deep convection (in terms of midtropospheric upward water flux) comes from isolated storms, which is consistent with observations that many isolated storms occur during the monsoon break near Darwin (e.g., May et al. 2008).

In contrast to T06MH, M0811MH has little water imbalance in the convective region, which implies that isolated storms contribute little to precipitation and therefore agrees with observations that 92% of the precipitation at Niamey came from MCSs during the AMMA SOP (Le Barbé and Lebel 1997; Guy et al. 2011). Because of the propagation of MCSs and strong

stratiform precipitation (or water content in the stratiform clouds), an advective water flux occurs from the nonprecipitating to the convective region, which explains the water imbalance in M0811MH (see footnote 1 for more discussion).

#### b. Stratiform water budgets

Precipitation amounts and areas between stratiform/anvil and convective clouds are contrasted using model and observational data. As shown in Table 2, the ratio between modeled stratiform and convective cloud areas is 4.1 in M0811MH, which is close to the value derived from the C-band radar at Niamey (i.e., 4.9 for 11 August and 5.7 for the whole SOP). The ratio in T06MH is 5.0, which is close to the 3.4 value estimated from TWP-ICE radar observations (Frederick and Schumacher 2008). Moreover, the ratio between anvil and convective cloud area in T06MH is 15.5—much larger than that in M0811MH (1.8), which is consistent with the radar–lidar observations of Protat et al. (2010) that the frequency of ice cloud occurrence is much larger over Darwin than over Niamey.

TABLE 2. Stratiform/anvil vs convective cloud ratios.

Case	Percentage of stratiform rain	Ratio between stratiform and convective cloud areas	Ratio between anvil and convective cloud areas
M0811MH	51.4%	4.1	1.8
M0719MH	59.5%	14.0	7.5
T06MH	41.4%	5.0	15.5

Although the stratiform area is relatively smaller in M0811MH than in T06MH, the water source (or deposition rate) in the mixed-phase cloud layer in the stratiform region is large (see Fig. 11). Since the deposition rate is directly proportional to vertical velocity, the difference in deposition amount in the mixed-phase cloud layer implies that the mesoscale ascent around deep convection is stronger in M0811MH than in T06MH.

The preceding analysis of water budgets depicts a difference in cloud ensembles between Niamey and Darwin. Deep convection near Darwin is relatively strong and is associated with extensive anvil area, whereas stratiform clouds around deep convection near Niamey are relatively stronger in terms of vertical velocity. *CloudSat* observations consistently show that West African anvils tend to be closely tied to the convective regions of MCSs (Cetrone and Houze 2009; Frey et al. 2011).

### 5. Discussion

The difference in convective, stratiform, and anvil clouds between the modeled AMMA and TWP-ICE MCSs is related to many factors. Two of them are vertical wind shear and dust particle concentration. Next, the three numerical experiments in Table 1 are compared with additional sensitivity experiments, addressing the effects of the two factors on stratiform and anvil clouds.

#### a. Vertical wind shear

Figure 13 displays vertical profiles of observed zonal and meridional velocity components averaged over the modeling periods. Since vertical wind shear at different heights affects stratiform and anvil clouds differently (e.g., Rotunno et al. 1988; Moncrieff 1992), two additional TWP-ICE experiments (i.e., T06MH1S and T06MH2S) are carried out to help examine the effects of the observed vertical wind shear on stratiform/anvil cloud area in AMMA and TWP-ICE MCSs.

To study the effect of upper-tropospheric (UT) vertical wind shear, experiment T06MH1S is conducted using the same setup as T06MH except for a vertical wind shear of zero above 290 hPa or 10 km (i.e., the horizontal wind components above the height of 290 hPa equal those at 290 hPa, respectively). In the experiment, the modeled convective, stratiform, and anvil clouds have slightly smaller, smaller, and almost the same areas as those in T06MH, respectively. Such differences in cloud areas between T06MH1S and T06MH imply that the UT vertical wind shear favors the formation of wide stratiform clouds.

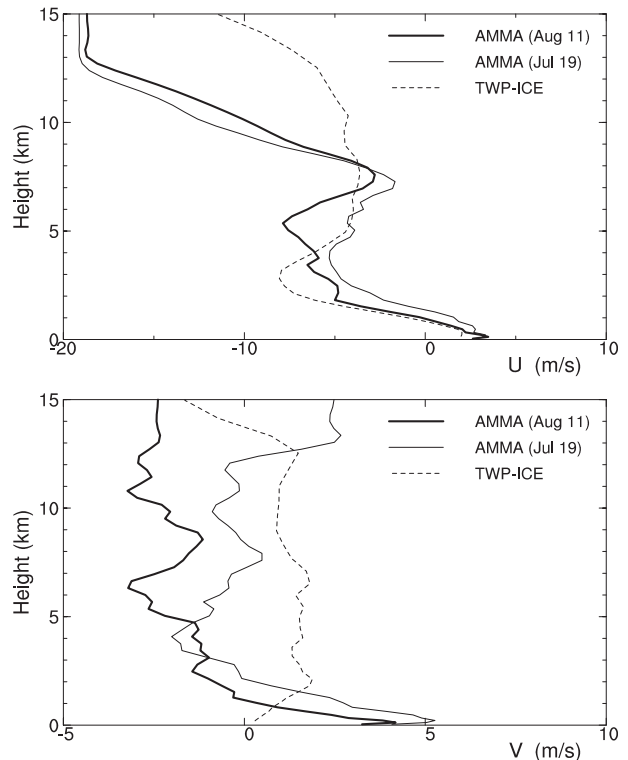


FIG. 13. Vertical profiles of the (top) zonal and (bottom) meridional wind components averaged over the modeling periods.

In contrast to T06MH1S, experiment T06MH2S uses the same setup as T06MH, but its vertical wind shear is decreased by half (or the horizontal wind components from the model bottom to top equal half of the observed, respectively). In this experiment, the modeled convective, stratiform, and anvil clouds have larger, obviously larger, and slightly smaller areas than those in T06MH, respectively. Such differences in cloud areas between T06MH2S and T06MH imply that the vertical wind shear in the middle and lower troposphere does not favor the formation of wide stratiform clouds.

Results from these two experiments are consistent with those from MCS observations and previous CRM simulations. Since deep convection brings about long-lasting stratiform clouds, the length (and therefore area) of stratiform clouds is directly proportional to the relative horizontal displacement of an UT air parcel with respect to deep convective cores or

$$\mathbf{v}_u - \mathbf{v}_d = (\mathbf{v}_u - \mathbf{v}_m) + (\mathbf{v}_m - \mathbf{v}_d), \quad (1)$$

where  $\mathbf{v}_u$  and  $\mathbf{v}_m$  denote the horizontal wind in the upper and middle troposphere, respectively, and  $\mathbf{v}_d$  the propagation velocity of deep convective cores.

The first term on the right-hand side of (1),  $\mathbf{v}_u - \mathbf{v}_m$ , denotes the effect of vertical wind shear on stratiform

clouds (e.g., Moncrieff 1992), and its effect is shown by the contrast between T06MH and T06MH1S. With the aid of this term, the difference in UT vertical wind shear shown in Fig. 13 can be used to partly explain the difference in stratiform and anvil clouds between AMMA and TWP-ICE MCSs.

The second term on the right-hand side of (1),  $\mathbf{v}_m - \mathbf{v}_d$ , can also be used to explain the difference in stratiform and anvil clouds between the modeled MCSs. Previous CRM simulations at radiative–convective equilibrium showed that clouds become organized and that these organized cloud systems propagate horizontally even without environmental vertical wind shear (e.g., Grabowski and Moncrieff 2004; Bretherton et al. 2005; Zeng et al. 2010). This suggests a complex relationship between MCS propagation (or  $\mathbf{v}_d$ ) and vertical wind shear. The area of stratiform clouds in T06MH2S is larger than that in T06MH, which implies that the propagation speed (or stratiform cloud area) of MCSs increases with decreasing vertical wind shear in the middle (and lower) troposphere.

Satellite observations of the 11 August and 19 July MCSs support the effect of vertical wind shear on MCS propagation speed. Figure 13 shows that vertical wind shear between 2 and 11 km in the 11 August MCS is larger than that in the 19 July MCS. Meanwhile, hourly *Meteosat-8* images show that new convective cells formed far ahead of the 19 July MCS (e.g., at 0200 UTC 19 July) so that the apparent propagation speed of the 19 July MCS is larger than that of the 11 August MCS. Such a difference in propagation speed can be used to explain the difference in stratiform cloud area between the 11 August and 19 July MCSs (see Table 2). Similarly, the vertical wind shear between 2 and 11 km in TWP-ICE is smaller than those in the two AMMA MCSs, which can be used to partly explain the larger area of stratiform and anvil clouds in T06MH (Protat et al. 2010; Table 2).

### b. Ice crystal concentration

Ice crystal concentration (ICC) or mineral particle concentration can affect MCSs, too. Dust particles were abundant over the Saharan desert during the SOP (Zipser et al. 2009). They were carried into the sounding network by northerly winds above about 2 km (see Fig. 13) and then entrained into clouds via low-level convergence below about 10 km (see Fig. 12). Aircraft observations showed that the highest ice particle concentrations observed at  $-44^\circ\text{C}$  occurred in the strongest updrafts and correlated well with observations of high aerosol loading in the boundary layer (Heymsfield et al. 2009; Bouniol et al. 2010). Hence, it is inferred that the ice nuclei concentrations (or ICC) in the AMMA clouds were higher than in those from TWP-ICE.

The effects of ICC on MCSs are revealed in the differences in MCS sizes and water budgets between AMMA and TWP-ICE, which is discussed next, beginning with an additional numerical experiment M0811L that follows the same setup as M0811MH except for using a low ICC. The microphysics scheme for M0811L is equivalent to the original Rutledge–Hobbs scheme that works well in midlatitudinal cloud simulations (e.g., Zeng et al. 2009b). Figure 14 displays the horizontal distributions of cloud ice at 8.6 km and graupel at 5 km at 0400 UTC 11 August from M0811L. It is contrasted against the results from M0811MH (Fig. 7), showing the effect of ICC on MCSs. Namely, a decrease in ICC leads to a significant decrease in the UT cloud ice amount and subsequently a decrease in MCS anvil/stratiform area, which suggests that abundant ice nuclei, such as was observed in AMMA, is one of the factors contributing to extensive MCSs over West Africa, in addition to other thermodynamic and dynamic factors.

The contrast of Figs. 7 and 14 shows a sensitivity of MCS size to ICC. Thus, the difference in ICC between AMMA and TWP-ICE clouds can be identified using MCS scale (instead of UT ice water content<sup>2</sup>) as a comparison standard. Radar and satellite observations show that the size of AMMA MCSs is larger than those in TWP-ICE (e.g., Frederick and Schumacher 2008), implying that the ICC in AMMA clouds is higher than that in TWP-ICE clouds.

The inferred difference in ICC between AMMA and TWP-ICE clouds is supported by the difference in water budgets between them. The water source in the mixed-phase region in the AMMA stratiform clouds, as shown by Fig. 11, is larger than that in the TWP-ICE ones. If an air parcel is used to understand the difference, its vertical velocity (or the mesoscale ascent around deep convection) in AMMA stratiform clouds must be larger than in those for TWP-ICE.

The difference in mesoscale ascent between AMMA and TWP-ICE stratiform clouds can be related to the

<sup>2</sup> In section 3b, the ice water content derived from the W-band radar was used to estimate the ICC just as was done in Zeng et al. (2011). When a high ice crystal concentration was used in M0811MH, the modeled UT ice water content is close to the observed. Such a high concentration, in comparison to the small one in M0811L, indicates that the ICC in AMMA clouds is much larger than that in midlatitudinal clouds, supporting the conclusion of Zeng et al. (2011). On the other hand, the estimated ICC in AMMA clouds is close to that in TWP-ICE, which implies that such estimation of ICC is not accurate enough to identify the difference in ICC between AMMA and TWP-ICE clouds. The inaccuracy of ICC estimation is attributed mainly to errors from the microphysics parameterization, such as that discussed in Powell et al. (2012) and section 3b.

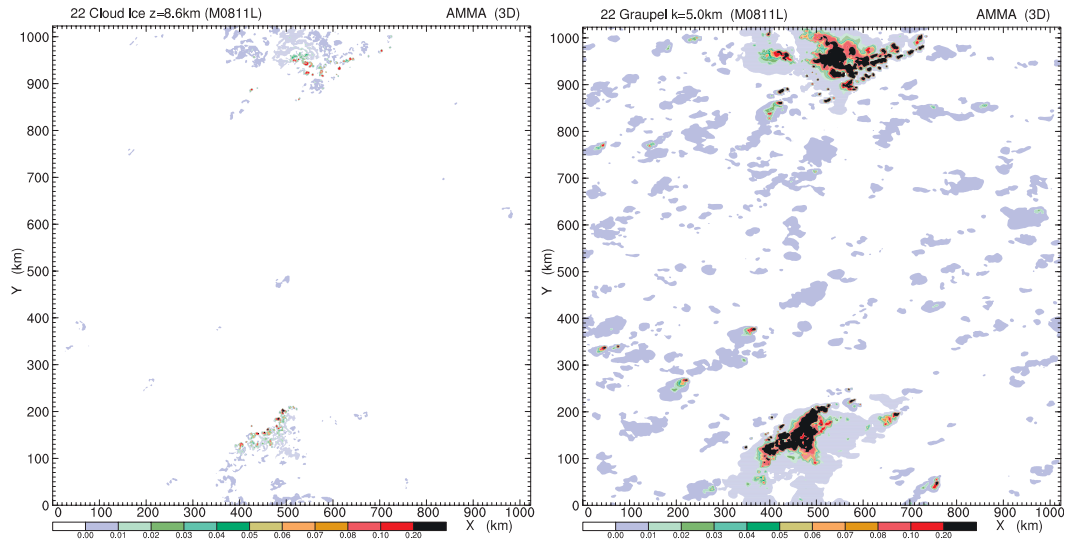


FIG. 14. As in Fig. 7, but for experiment M0811L that uses the Rutledge and Hobbs (1984) scheme, which results in a low ice crystal concentration.

difference in ICC between AMMA and TWP-ICE clouds. At the radiative–convective equilibrium in horizontally uniform environments, mesoscale ascent works as a dynamic factor to organize clouds no matter how they draw energy from their environment (e.g., Grabowski and Moncrieff 2004; Bretherton et al. 2005; Zeng et al. 2010). Owing to the connection between cloud organization and mesoscale ascent, the effect of cloud microphysics on cloud organization provides information on the effect of cloud microphysics on mesoscale ascent. The sensitivity experiments of Zeng et al. (2010) showed that clouds are organized well when the microphysics parameterization for cold clouds (with “high” ICC) is used and are organized weakly (or isolated) when the parameterization for warm clouds (with zero ICC) is used. This result implies that mesoscale ascent around deep convection becomes stronger with increasing ICC, which is consistent with the difference in water budgets,<sup>3</sup> the difference in mineral dust concentration between AMMA and TWP-ICE clouds (see [http://eosweb.larc.nasa.gov/HPDOCS/misr/misr\\_html/global\\_aerosols.html](http://eosweb.larc.nasa.gov/HPDOCS/misr/misr_html/global_aerosols.html)), and the satellite observations of Cetrone and Houze (2009) that West African anvils tend to be closely tied to the convective regions of MCSs.

<sup>3</sup> Suppose that mineral particle concentration (or ICC) can impact atmospheric temperature and humidity via clouds. Thus, the AMMA sounding network can detect information on the effect of mineral particles on atmospheric variables that will be reflected in the computed water budgets.

## 6. Concluding remarks

Two climatological regimes, West Africa and the Maritime Continent, possess different cloud ensembles with West African anvils tending to be closely tied to the convective regions of MCSs (Cetrone and Houze 2009). Ground-based radar and lidar from two sites (Niamey and Darwin) within these two regimes reveal that the frequency of ice cloud occurrence is much lower over Niamey when compared to Darwin (Protat et al. 2010).

Two international field campaigns, AMMA and TWP-ICE, with upper-air sounding networks took place around the two sites, respectively, providing observational data to drive and evaluate CRM simulations. If the corresponding CRM simulations can duplicate the cloud characteristics observed in the two climatological regimes, they can then be used, as examples, to infer the factors that cause the difference in clouds between the two regimes.

In this paper, two MCSs observed during AMMA are modeled and contrasted against a population of MCSs from TWP-ICE. The modeled AMMA MCSs have a scale of about 400 km, consisting of convective, stratiform, and anvil clouds. They evolve from several smaller cloud systems. In their mature stage, each MCS has two deep convective regions, connected by anvil clouds (i.e., the two convective regions share the same cloud shield). These modeling characteristics resemble the radar and satellite observations of the real MCSs.

Water budgets for all of the modeled AMMA and TWP-ICE clouds are analyzed to show their difference

in clouds. The budgets are expressed in terms of horizontal water fluxes between the convective, stratiform, and anvil regions; the vertical water fluxes between warm, mixed-phase, and icy cloud layers; and water sources due to microphysical processes. The budgets were normalized by the total precipitation amount to facilitate a comparison of the water budget between the different geographic regions as well as to provide information to help determine the parameters in convective and cloud parameterization in general circulation models (GCMs).

A comparison of the water budgets between the modeled AMMA and TWP-ICE clouds showed that MCSs dominated the precipitation in AMMA while other cloud systems (e.g., isolated convective clouds) contributed significantly to the precipitation in TWP-ICE. This agrees with satellite and radar observations that most of the precipitation came from MCSs at Niamey during the AMMA SOP (Guy et al. 2011) while many isolated storms occurred during the monsoon break near Darwin (e.g., May et al. 2008). The water budget comparison also suggests that ascent in TWP-ICE convective clouds is stronger while the mesoscale ascent outside of convective clouds in AMMA is stronger, which is consistent with the observations of Cetrone and Houze (2009) and Protat et al. (2010) that the frequency of ice cloud occurrence is much lower over Niamey when compared to Darwin.

The numerical experiments are also compared with additional sensitivity tests to examine the effects of vertical wind shear and ice crystal concentration on MCSs. Strong vertical wind shear in the upper troposphere and weak shear in the middle and lower troposphere in TWP-ICE can explain the high frequency of ice clouds observed at Darwin. An increase in ice crystal concentration can bring about an increase in cloud shield area, which implies that high ice crystal concentrations are one of the key factors that contribute to the large MCSs in AMMA.

*Acknowledgments.* The authors appreciate the hard work and effort of all those who planned and participated in the AMMA SOP and TWP-ICE field campaigns. They acknowledge the NASA Ames Research

Center and the NASA Goddard Space Flight Center for the computer time used in this research. They thank Dr. Karen Mohr for her discussions on African cloud modeling and analysis, Chunpeng Wang for creating Figs. 8 and 10, and Stephen Lang for reading the manuscript. They also thank three anonymous reviewers for their critical yet constructive comments. Special thanks are extended to Dr. Wojciech Grabowski for his kind comments.

This research was supported by the Office of Science (BER), U.S. Department of Energy/Atmospheric System Research (DOE/ASR) Interagency Agreement DE-AI02-04ER63755. It was also supported by the NASA MAP project under Grants NNX09AJ46G and NNX10AG18G. Dr. W.-K. Tao was mainly supported by the NASA Precipitation Measurement Mission (PMM) and NASA Modeling Analysis Prediction (MAP).

## APPENDIX

### Computing Water Budgets

This appendix presents the algorithm on how to compute water budgets. Consider a governing equation for a water species

$$\frac{\partial[\rho\phi^{(m)}]}{\partial t} + \nabla \cdot [\mathbf{v}_h\rho\phi^{(m)}] + \frac{\partial[w\rho\phi^{(m)}]}{\partial z} = \rho S_{\phi^{(m)}}, \quad (\text{A1})$$

where  $\phi^{(m)}$  is the mixing ratio of a water species, with  $m = 1, 2, 3, 4,$  and  $5$  for cloud water, rainwater, cloud ice, snow, and graupel, respectively;  $\rho$  is air density;  $\mathbf{v}_h$  the horizontal wind vector;  $w$  the vertical velocity of a water species that includes its terminal velocity;  $S_{\phi^{(m)}}$  the source term of  $\phi^{(m)}$  from microphysical processes;  $t$  time; and  $z$  height. The equation ignores the term from sub-grid turbulence or motions.

Integrating (A1) over a given volume (e.g., those in Fig. 1) and a period yields the equation for the water budget. With the aid of the divergence theorem, integrating (A1) from time 0 to  $T$ , height  $z_1$  to  $z_2$ , then over a horizontal area enclosed by line  $L$ , and finally summing the resulting equation with  $m$  from 1 to 5 gives

$$\begin{aligned} & \iint_{x,y} \int_{z_1}^{z_2} \sum_{m=1}^5 [\rho\phi^{(m)}] \Big|_{t=0}^{t=T} dx dy dz + \int_{z_1}^{z_2} \int_0^T \oint_{\text{line } L} \sum_{m=1}^5 [\mathbf{v}_h\rho\phi^{(m)}] \cdot d\mathbf{L} dz dt + \iint_{x,y} \int_0^T \sum_{m=1}^5 [w\rho\phi^{(m)}] \Big|_{z=z_1}^{z=z_2} dx dy dt \\ & = \iint_{x,y} \int_{z_1}^{z_2} \int_0^T \sum_{m=1}^5 [\rho S_{\phi^{(m)}}] dx dy dz dt, \end{aligned} \quad (\text{A2})$$

where  $d\mathbf{L}$  represents an infinitesimal element of line  $L$ , whose magnitude is the length of the element and whose direction is perpendicular to the element. The first term on the left-hand side of (A2) is negligible for long-term integration, especially when the modeling period spans the life cycles of cloud systems.

The total precipitation amount that reaches the ground  $R$  (or  $R_c + R_s$  in Fig. 1) is expressed as

$$\begin{aligned} & \frac{1}{TR} \iint_{x,y} \int_0^T \sum_{m=1}^5 [w\rho\phi^{(m)}] \Big|_{z=z_2} dx dy dt - \frac{1}{TR} \iint_{x,y} \int_0^T \sum_{m=1}^5 [w\rho\phi^{(m)}] \Big|_{z=z_1} dx dy dt \\ & + \frac{1}{TR} \int_{z_1}^{z_2} \int_0^T \oint_{\text{line}L} \sum_{m=1}^5 [\mathbf{v}_h \rho \phi^{(m)}] \cdot d\mathbf{L} dz dt = \frac{1}{TR} \iint_{x,y} \int_{z_1}^{z_2} \int_0^T \sum_{m=1}^5 [\rho S_{\phi^{(m)}}] dx dy dz dt, \end{aligned} \quad (\text{A4})$$

where a term corresponds to a number in the water budgets of Fig. 11. Specifically, the term on the right-hand side of (A4) represents the water source from microphysical processes. The first two terms on the left-hand side represent the vertical transport of water at the top and bottom of a given volume, respectively. The third term on the left-hand side represents the horizontal transport of water from the given volume, and is further broken into several terms next.

The model domain is divided into four regions: convective, stratiform, anvil cloud, and clear-sky regions. When (A4) is applied to a region, there is a budget balance of water for the region. Since the current model is represented in the Cartesian coordinate system ( $x$ ,  $y$ ,  $z$ ) and its cells are cubical,  $d\mathbf{L}$  in (A4) is chosen to follow the edge of the boundary cells of a given region on a horizontal plane, simplifying the computation of the water budgets.

The third term on the left-hand side of (A4), or the horizontal transport of water between regions, can be further divided into terms from one region to another. Once the domain is divided into convective, stratiform, and anvil cloud and clear-sky regions, the horizontal transport of water between the regions is marked with its source and target regions and is then output in the form of Fig. 11.

#### REFERENCES

- Blossey, P. N., C. S. Bretherton, J. Cetrone, and M. Kharoutdino, 2007: Cloud-resolving model simulations of KWAJEX: Model sensitivities and comparisons with satellite and radar observations. *J. Atmos. Sci.*, **64**, 1488–1508.
- Bouniol, D., J. Delanoë, C. Duroure, A. Protat, V. Giraud, and G. Penide, 2010: Microphysical characterisation of West African MCS anvils. *Quart. J. Roy. Meteor. Soc.*, **136**, 323–344.
- Bretherton, C. S., P. N. Blossey, and M. Khairoutdinov, 2005: An energy-balance analysis of deep convective self-aggregation above uniform SST. *J. Atmos. Sci.*, **62**, 4273–4292.
- Caniaux, G., J.-L. Redelsperger, and J.-P. Lafore, 1994: A numerical study of the stratiform region of a fast-moving squall line. Part I: General description of water and heat budgets. *J. Atmos. Sci.*, **51**, 2046–2074.
- Cetrone, J., and R. A. Houze Jr., 2009: Anvil clouds of tropical mesoscale convective systems in monsoon regions. *Quart. J. Roy. Meteor. Soc.*, **135**, 305–317.
- , and —, 2011: Leading and trailing anvil clouds of West African squall lines. *J. Atmos. Sci.*, **68**, 1114–1123.
- Chin, H.-N. S., 1994: The impact of the ice phase and radiation on a midlatitude squall line system. *J. Atmos. Sci.*, **51**, 3320–3343.
- Churchill, D. D., and R. A. Houze Jr., 1984: Development and structure of winter monsoon cloud clusters on 10 December 1978. *J. Atmos. Sci.*, **41**, 933–960.
- Frederick, K., and C. Schumacher, 2008: Anvil characteristics as seen by C-POL during the Tropical Warm Pool International Cloud Experiment (TWP-ICE). *Mon. Wea. Rev.*, **136**, 206–222.
- Frey, W., and Coauthors, 2011: In situ measurements of tropical cloud properties in the West African Monsoon: Upper tropospheric ice clouds, Mesoscale Convective System outflow, and subvisual cirrus. *Atmos. Chem. Phys.*, **11**, 5569–5590.
- Gamache, J. F., and R. A. Houze Jr., 1983: Water budget of a mesoscale convective system in the tropics. *J. Atmos. Sci.*, **40**, 1835–1850.
- Grabowski, W. W., and M. W. Moncrieff, 2004: Moisture-convection feedback in the tropics. *Quart. J. Roy. Meteor. Soc.*, **130**, 3081–3104.
- , X. Wu, and M. W. Moncrieff, 1996: Cloud resolving modeling of tropical cloud systems during Phase III of GATE. Part I: Two-dimensional experiments. *J. Atmos. Sci.*, **53**, 3684–3709.
- , —, —, and D. Hall, 1998: Cloud-resolving modeling of cloud systems during Phase III of GATE. Part II: Effects of resolution and the third spatial dimension. *J. Atmos. Sci.*, **55**, 3264–3282.
- Guy, N., S. A. Rutledge, and R. Cifelli, 2011: Radar characteristics of continental, coastal, and maritime convection observed during AMMA/NAMMA. *Quart. J. Roy. Meteor. Soc.*, **137**, 1241–1256.

- Heymsfield, A. J., A. Bansemer, G. Heymsfield, and A. O. Fierro, 2009: Microphysics of maritime tropical convective updrafts at temperatures from  $-20^{\circ}$  to  $-60^{\circ}$ . *J. Atmos. Sci.*, **66**, 3530–3562.
- Houze, R. A., Jr., 1977: Structure and dynamics of a tropical squall line system. *Mon. Wea. Rev.*, **105**, 1540–1567.
- , 1982: Cloud clusters and large-scale vertical motion in the tropics. *J. Meteor. Soc. Japan*, **60**, 396–410.
- , 1997: Stratiform precipitation in regions of convection: A meteorological paradox. *Bull. Amer. Meteor. Soc.*, **78**, 2179–2196.
- , 2004: Mesoscale convective systems. *Rev. Geophys.*, **42**, RG4003, doi:10.1029/2004RG000150.
- , C.-P. Cheng, C. A. Leary, and J. F. Gamache, 1980: Diagnosis of cloud mass and heat fluxes from radar and synoptic data. *J. Atmos. Sci.*, **37**, 754–773.
- Huffman, G. J., and Coauthors, 2007: The TRMM Multisatellite Precipitation Analysis (TMPA): Quasi-global, multiyear, combined-sensor precipitation estimates at fine scales. *J. Hydrometeorol.*, **8**, 38–55.
- Johnson, D. E., W.-K. Tao, J. Simpson, and C.-H. Sui, 2002: A study of the response of deep tropical clouds to large-scale thermodynamic forcing. Part I: Modeling strategies and simulations of TOGA COARE convective systems. *J. Atmos. Sci.*, **59**, 3492–3518.
- Johnson, R. H., and P. J. Hamilton, 1988: The relationship of surface pressure features to the precipitation and airflow structure of an intense midlatitude squall line. *Mon. Wea. Rev.*, **116**, 1444–1471.
- Klemp, J. B., and R. B. Wilhelmson, 1978: The simulation of three-dimensional convective storm dynamics. *J. Atmos. Sci.*, **35**, 1070–1096.
- Lang, S., W.-K. Tao, J. Simpson, and B. Ferrier, 2003: Modeling of convective–stratiform precipitation processes: Sensitivity to partitioning methods. *J. Appl. Meteor.*, **42**, 505–527.
- Leary, C. A., and R. A. Houze Jr., 1979: The structure and evolution of convection in a tropical cloud cluster. *J. Atmos. Sci.*, **36**, 437–457.
- Le Barbé, L., and T. Lebel, 1997: Rainfall climatology of the HAPEX-Sahel region during the years 1950–1990. *J. Hydrol.*, **188**, 43–73.
- Loehrer, S. M., T. A. Edmands, and J. A. Moore, 1996: TOGA COARE upper-air sounding data archive: Development and quality control procedures. *Bull. Amer. Meteor. Soc.*, **77**, 2651–2671.
- Matsui, T., X. Zeng, W.-K. Tao, H. Masunaga, W. Olson, and S. Lang, 2009: Evaluation of long-term cloud-resolving model simulations using satellite radiance observations and multi-frequency satellite simulators. *J. Atmos. Oceanic Technol.*, **26**, 1261–1274.
- May, P. T., J. H. Mather, G. Vaughan, C. Jakob, G. M. McFarquhar, K. N. Bower, and G. G. Mace, 2008: The Tropical Warm Pool International Cloud Experiment. *Bull. Amer. Meteor. Soc.*, **89**, 629–645.
- Mohr, K. I., and E. J. Zipser, 1996: Mesoscale convective systems defined by their 85-GHz ice scattering signature: Size and intensity comparison over tropical oceans and continents. *Mon. Wea. Rev.*, **124**, 2417–2437.
- Moncrieff, M. W., 1992: Organized convective systems: Archetypal dynamical models, mass and momentum flux theory, and parameterization. *Quart. J. Roy. Meteor. Soc.*, **118**, 819–850.
- Morrison, H., and Coauthors, 2011: Intercomparison of cloud model simulations of Arctic mixed-phase boundary layer clouds observed during SHEBA/FIRE-ACE. *J. Adv. Model. Earth Syst.*, **3**, M06003, doi:10.1029/2011MS000066.
- Nesbitt, S. W., E. J. Zipser, and D. J. Cecil, 2000: A census of precipitation features in the tropics using TRMM: Radar, ice scattering, and lighting observations. *J. Climate*, **13**, 4087–4106.
- Nuret, M., J.-P. Lafore, O. Bock, F. Guichard, A. Agusti-Panareda, J.-B. N’Gamini, and J.-L. Redelsperger, 2008: Correction of humidity bias for Vaisala RS80-A sondes during AMMA 2006 observing period. *J. Atmos. Oceanic Technol.*, **25**, 2152–2158.
- Phillips, V. T. J., and L. J. Donner, 2006: Cloud microphysics, radiation and vertical velocities in two- and three-dimensional simulations of deep convection. *Quart. J. Roy. Meteor. Soc.*, **132**, 3011–3033.
- Powell, S. W., R. A. Houze Jr., A. Kumar, and S. A. McFarlane, 2012: Comparison of simulated and observed continental tropical anvil clouds and their radiative heating profiles. *J. Atmos. Sci.*, **69**, 2662–2681.
- Protat, A., J. Delanoë, A. Plana-Fattori, P. T. May, and E. J. O’Connor, 2010: The statistical properties of tropical ice clouds generated by the West African and Australian monsoons, from ground-based radar–lidar observations. *Quart. J. Roy. Meteor. Soc.*, **136**, 345–363.
- Redelsperger, J.-L., C. D. Thorncroft, A. Diedhiou, T. Lebel, D. J. Parker, and J. Polcher, 2006: African Monsoon Multi-disciplinary Analysis: An international research project and field campaign. *Bull. Amer. Meteor. Soc.*, **87**, 1739–1746.
- Rotunno, R., J. B. Klemp, and M. L. Weisman, 1988: A theory for strong, long-lived squall lines. *J. Atmos. Sci.*, **45**, 463–485.
- Rutledge, S. A., and P. V. Hobbs, 1984: The mesoscale and microscale structure and organization of clouds and precipitation in mid-latitude clouds. Part XII: A diagnostic modeling study of precipitation development in narrow cold frontal rainbands. *J. Atmos. Sci.*, **41**, 2949–2972.
- , and R. A. Houze Jr., 1987: A diagnostic modeling study of the trailing stratiform rain of a midlatitude squall line. *J. Atmos. Sci.*, **44**, 2640–2656.
- Schumacher, C., and R. A. Houze Jr., 2006: Stratiform precipitation production over sub-Saharan Africa and the tropical East Atlantic as observed by TRMM. *Quart. J. Roy. Meteor. Soc.*, **132**, 2235–2255.
- Smolarkiewicz, P. K., and W. W. Grabowski, 1990: The multi-dimensional positive advection transport algorithm: Non-oscillatory option. *J. Comput. Phys.*, **86**, 355–375.
- Soong, S.-T., and Y. Ogura, 1980: Response of tradewind cumuli to large-scale processes. *J. Atmos. Sci.*, **37**, 2035–2050.
- Stephens, G. L., and Coauthors, 2002: The *CloudSat* mission and the A-Train: A new dimension to space-based observations of clouds and precipitation. *Bull. Amer. Meteor. Soc.*, **83**, 1771–1790.
- Tao, W.-K., 2003: Goddard Cumulus Ensemble (GCE) model: Application for understanding precipitation processes. *Meteor. Monogr.*, No. 51, Amer. Meteor. Soc., 107–138.
- , and J. Simpson, 1993: The Goddard Cumulus Ensemble model. Part I: Model description. *Terr. Atmos. Ocean. Sci.*, **4**, 19–54.
- , —, C. H. Sui, B. Ferrier, S. Lang, J. Scala, M. D. Chou, and K. Pickering, 1993: Heating, moisture, and water budgets of tropical and midlatitude squall lines: Comparisons and sensitivity to longwave radiation. *J. Atmos. Sci.*, **50**, 673–690.

- , S. Lang, J. Simpson, C.-H. Sui, B. Ferrier, and M.-D. Chou, 1996: Mechanisms of cloud–radiation interaction in the tropics and midlatitudes. *J. Atmos. Sci.*, **53**, 2624–2651.
- , and Coauthors, 2003: Microphysics, radiation and surface processes in the Goddard Cumulus Ensemble (GCE) model. *Meteor. Atmos. Phys.*, **82**, 97–137.
- Wu, X., and M. W. Moncrieff, 2001: Long-term behavior of cloud systems in TOGA COARE and their interactions with radiative and surface processes. Part III: Effects on the energy budget and SST. *J. Atmos. Sci.*, **58**, 1155–1168.
- , W. D. Hall, W. W. Grabowski, M. W. Moncrieff, W. D. Collins, and J. T. Kiehl, 1999: Long-term behavior of cloud systems in TOGA COARE and their interactions with radiative and surface processes. Part II: Effects of ice microphysics on cloud–radiation interaction. *J. Atmos. Sci.*, **56**, 3177–3195.
- Xie, S., T. Hume, C. Jakob, S. Klein, R. McCoy, and M. Zhang, 2010: Observed large-scale conditions and diabatic heating and drying profiles during TWP-ICE. *J. Climate*, **23**, 57–79.
- Xu, K.-M., and D. A. Randall, 1996: Explicit simulation of cumulus ensembles with the GATE Phase III data: Comparison with observations. *J. Atmos. Sci.*, **53**, 3710–3736.
- , and Coauthors, 2005: Modeling springtime shallow frontal clouds with cloud-resolving and single-column models. *J. Geophys. Res.*, **110**, D15S04, doi:10.1029/2004JD005153.
- Yuan, J., and R. A. Houze Jr., 2010: Global variability of mesoscale convective system anvil structure from A-train satellite data. *J. Climate*, **23**, 5864–5888.
- Zeng, X., and Coauthors, 2007: Evaluating clouds in long-term cloud-resolving model simulations with observational data. *J. Atmos. Sci.*, **64**, 4153–4177.
- , W.-K. Tao, S. Lang, A. Y. Hou, M. Zhang, and J. Simpson, 2008: On the sensitivity of atmospheric ensembles to cloud microphysics in long-term cloud-resolving model simulations. *J. Meteor. Soc. Japan*, **86A**, 45–65.
- , and Coauthors, 2009a: A contribution by ice nuclei to global warming. *Quart. J. Roy. Meteor. Soc.*, **135**, 1614–1629.
- , and Coauthors, 2009b: An indirect effect of ice nuclei on atmospheric radiation. *J. Atmos. Sci.*, **66**, 41–61.
- , W.-K. Tao, and R. A. Houze Jr., cited 2010: Modeling mesoscale convective systems in a highly simplified environment. [Available online at [http://asr.science.energy.gov/meetings/stm/posters/poster\\_pdf/2010/P000163.pdf](http://asr.science.energy.gov/meetings/stm/posters/poster_pdf/2010/P000163.pdf).]
- , —, T. Matsui, S. Xie, S. Lang, M. Zhang, D. Starr, and X. Li, 2011: Estimating the ice crystal enhancement factor in the tropics. *J. Atmos. Sci.*, **68**, 1424–1434.
- Zipser, E. J., 1969: The role of organized unsaturated convective downdrafts in the structure and rapid decay of an equatorial disturbance. *J. Appl. Meteor.*, **8**, 799–814.
- , 1977: Mesoscale and convective-scale downdrafts as distinct components of squall-line circulation. *Mon. Wea. Rev.*, **105**, 1568–1589.
- , R. J. Meitin, and M. A. LeMone, 1981: Mesoscale motion fields associated with a slowly moving GATE convective band. *J. Atmos. Sci.*, **38**, 1725–1750.
- , and Coauthors, 2009: The Saharan air layer and the fate of African easterly waves—NASA’s AMMA field study of tropical cyclogenesis. *Bull. Amer. Meteor. Soc.*, **90**, 1137–1156.